JGR Space Physics

RESEARCH ARTICLE
10.1029/2020JA028205

A Case Study on the Origin of Near-Earth Plasma

A. Glocer[1], D. Welling[2], C. R. Chappell[3], G. Toth[4], M.-C. Fok[1], C. Komar[1,5], S.-B. Kang[1,5], N. Buzulukova[1,6], C. Ferradas[1,5], S. Bingham[7,†], and C. Mouikis[8]

[1]NASA/GSFC, Greenbelt, MD, USA, [2]Department of Physics, University of Texas at Arlington, Arlington, TX, USA, [3]Vanderbilt University, Nashville, TN, USA, [4]Climate and Space Sciences and Engineering, University of Michigan, Ann Arbor, MI, USA, [5]Catholic University of America, Washington D.C, USA, [6]University of Maryland, College Park, MD, USA, [7]Applied Physics Laboratory (Deceased), Johns Hopkins University, Laurel, MD, USA, [8]Space Science Center, University of New Hampshire, Durham, NH, USA

†Deceased 4 July 2020

Key Points:

- Ionospheric H^+ is a critically important contributor to the magnetosphere during a storm
- Seasonal effect on outflow create asymmetric filling of the lobes
- The inclusion of an additional plasmaspheric fluid has system-wide effects

Correspondence to:
A. Glocer,
alex.glocer-1@nasa.gov

Citation:
Glocer, A., Welling, D., Chappell, C. R., Toth, G., Fok, M.-C., Komar, C., et al. (2020). A case study on the origin of near-Earth plasma. *Journal of Geophysical Research: Space Physics*, *125*, e2020JA028205. https://doi.org/10.1029/2020JA028205

Received 8 MAY 2020
Accepted 28 SEP 2020
Accepted article online 10 OCT 2020

Abstract This study presents simulations of the coupled space environment during a geomagnetic storm that separates the different sources of near-Earth plasma. These simulations include separate fluids for solar wind and ionospheric protons, ionospheric oxygen, and the plasmasphere. Additionally, they include the effects of both a hot ring current population and a cold plasmaspheric population simultaneously for a geomagnetic storm. The modeled ring current population represents the solution of bounce-averaged kinetic solution; the core plasmaspheric model assumes a fixed temperature of 1 eV and constant pressure along the field line. We find that during the storm, ionospheric protons can be a major contributor to the plasmasheet and ring current and that ionospheric plasma can largely displace solar wind protons in much of the magnetosphere under certain conditions. Indeed, the ionospheric source of plasma cannot be ignored. Significant hemispheric asymmetry is found between the outflow calculated in the summer and winter hemispheres, consistent with past observations. That asymmetric outflow is found to lead to asymmetric filling of the lobes, with the northern (summer) lobe receiving more outflow that has a higher proportion of O^+ and the southern (winter) lobe receiving less outflow with a higher proportion of H^+. We moreover find that the inclusion of the plasmasphere can have a system-wide impact. Specifically, when the plasmasphere drainage plume reaches the magnetopause, it can reduce the reconnection rate, suppress ionospheric outflow and change its composition, change the composition in the magnetosphere, and reduce the ring current intensity.

1. Introduction

Throughout much of the early space age, it was generally accepted that the solar wind was the source of most of the magnetospheric plasma, with the exception of the plasmasphere, which had a composition and temperature matching the underlying ionosphere. That assumption began to change in the early 1970s, first with the discovery of the H^+ polar wind by the Explorer 31 and ISIS 2 satellites (Brinton et al., 1971; Hoffman, 1970; Hoffman et al., 1974) and then with the observation of energetic O^+ raining down out of the magnetosphere (Shelley et al., 1972). These latter observations were particularly compelling as the ionosphere is the only source of O^+, and its presence therefore constitutes unambiguous proof of the ionospheric supply of plasma to the magnetosphere. It has since been argued that plasma of ionospheric origin is pervasive throughout geospace and may at times be the dominant source of plasma in the magnetosphere (Chappell et al., 1987; Lennartsson et al., 1981). Since these discoveries, the origin of near-Earth plasma and the relative importance of the solar wind and ionosphere to its supply has been an area of fundamental importance and keen scientific interest.

In the study of ionospheric outflow, there is often a disproportionate focus on heavy O^+ ions as opposed to the lighter protons. The emphasis on O^+ is understandable as it is clear evidence of ionospheric outflow, but it can give the mistaken impression that protons in the magnetosphere are primarily from the solar wind. While it is true that solar wind protons enter the magnetosphere via reconnection and interaction on the flanks, they are also constantly flowing out of the high-latitude ionosphere via the polar wind and filling the lobes (e.g., Axford, 1968). Indeed, Seki et al. (2003) postulated, and recent observations from the Cluster satellites demonstrate, that there is a significant cold population of ionospheric plasma in the magnetosphere

(Andre & Cully, 2012; Engwall et al., 2009). This initially cold population does not necessarily remain cold and may gain significant energy in the magnetosphere and contribute significantly to the magnetospheric proton population. This fact was demonstrated by Huddleston et al. (2005) by combining observed polar wind H^+ from the Polar satellite with simulated particle tracing in empirical magnetic fields. They showed that a polar wind proton starting at less than 1 eV was able to gain multiple keV of energy by the time it reached the plasmasheet and ring current.

Further complicating this picture is that it is impossible to determine the origin of any particular proton observed in the magnetosphere. However, it is possible to gain some understanding of the origin of magnetospheric protons in the aggregate using observations. One technique involves comparing the ratio of protons to other minor ions in the solar wind and assuming that similar ratios hold for solar wind protons that make it into the magnetosphere. Using this approach, Gloeckler and Hamilton (1987) estimate that as much as 65% of the proton population in the magnetosphere during geomagnetic storms is of ionospheric origin. Additional estimations of the fraction of geogenic plasma in the plasmasheet are discussed by Peterson (2002). One of the studies discussed, from Shelley et al. (1986) and Shelley (1986), estimates that under 10% of plasma in the plasmasheet originates in the ionosphere during quiet times, but that fraction rises to more than 50% during active times, which is consistent with the estimate of Gloeckler and Hamilton (1987). A number of assumptions go into this estimate, but of particular relevance to the present discussion is that they separate the ionospheric and solar wind protons by combining the empirical ratio of escaping H^+ and O^+ with the oxygen ion density in the plasmasheet.

Aside from observations, global models have proven to be a valuable tool in the study of the origin of near-Earth plasma. These models can be loosely broken down into two categories. The first category involves models that track large numbers of test particles, launched from the ionosphere, through either empirical or single fluid magnetohydrodynamic (MHD) fields (e.g., Moore et al., 2005; Peroomian et al., 2007). This approach does not allow particles and fields to evolve self-consistently but has advantage of including kinetic effects or non-Maxwellian particle distributions. The second category involves using a fluid approach to track each source of plasma separately, which has the advantage of allowing the plasma and the fields to evolve in a consistent manner. This technique can use multiple continuity equations and a single momentum equation (Glocer et al., 2009; Welling et al., 2011) or can involve multiple continuity, momentum, and energy equations in a true multifluid MHD magnetosphere model (e.g., Glocer et al., 2009; Wiltberger et al., 2010; Winglee et al., 2002).

While these previous approaches have advanced our knowledge of the effect of ionospheric plasma on the magnetosphere, they all suffer from significant shortcomings. Ideally, a global model with an ionospheric source of plasma would include a separate solar wind and polar wind proton population, a self-consistent ring current, and separate outflow representations for each hemisphere. While some models in the literature include some subset of these features, no model includes them all. Moreover, while there are global magnetosphere models that include a cold dense plasmasphere population (e.g., Ouellette et al., 2016; Zhang et al., 2016) or a ring current population (e.g., De Zeeuw et al., 2004; Glocer et al., 2013), there is not yet a published model that includes both of these hot and cold populations simultaneously. This is a particularly troublesome problem as the plasmasphere population carries much of the mass density in the inner magnetosphere, whereas the ring current carries much of the energy density in the magnetosphere. Choosing to only represent one population or the other means that significant physical effects may go uncaptured.

In this paper, we advance the current state-of-the-art by introducing new modeling capabilities to address many of the shortcomings described above. The model presented here builds on the recent work to separately track ionospheric and solar wind plasma while simultaneously including hemispheric asymmetry in the outflow, which is critical to capturing seasonal effects. The model also includes a multicomponent hot ring current and cold plasmaspheric population in the global magnetosphere. We describe these advances in section 2 and apply the model to a particular geomagnetic storm in sections 3 and 4. Discussion of the results is given in section 5.

2. Modeling Approach for Separating the Sources of Magnetospheric Plasma

The starting point for the modeling approach described in this paper is the configuration described by Glocer et al. (2018). In that study, a multifluid MHD code (Block-Adaptive-Tree Solar-wind Roe-type Upwind

Scheme [BATS-R-US]) was combined with a fluid-kinetic outflow model (PWOM) and a bounce-averaged kinetic ring current model (CIMI). These models are coupled together via the Space Weather Modeling Framework (SWMF), exchanging information at a frequent cadence (Tóth et al., 2012). This setup allows for a first principles representation of outflow and the ability to track different plasma populations through the magnetosphere and into the ring current. We build on this setup by adding three new key features. First, the proton population is separated into solar wind and polar wind protons. Second, a separate plasmasphere fluid is included to enable the hot ring current and cold plasmasphere to both be represented in the inner magnetosphere. Finally, separate outflow solutions for the Northern and Southern Hemispheres are included to allow for the study of hemispheric asymmetry of outflow on the magnetosphere. In the following sections, we provide a brief summary of each of the models used in the present study.

2.1. The PWOM

The Polar Wind Outflow Model (PWOM) (Glocer et al., 2007, 2009; Gombosi & Nagy, 1989) represents the high-latitude ionospheric source of plasma in this study. It provides a first principles calculation of ionospheric outflow, determining the solution of ionospheric H^+, O^+, He^+, and electrons in the transition region between the magnetosphere and ionosphere. The lower bound of the PWOM is located in the ionosphere below the F2 peak (altitude = 200 km), while the upper boundary is in the magnetosphere at a few Earth radii. The complete 3-D solution is obtained by multiple field-aligned solutions along field lines convecting through the polar cap. Recently, the model has been expanded to include a number of new features. These include the effect of superthermal electrons (Glocer et al., 2012, 2017), as well as a transition to kinetic ions at high altitudes using a hybrid macroscopic particle-in-cell (Mac-PIC) technique (Glocer et al., 2018).

Superthermal electrons are critical to the modeling ionospheric outflow and were first added to PWOM by Glocer et al. (2012) with results found to be in excellent agreement with observations. Since that time, a fully kinetic treatment of superthermal electrons has been added (Glocer et al., 2017), as well as a two-stream representation (Glocer et al., 2018) based on an adapted implementation of the GLOW code (Solomon, 2017; Solomon et al., 1988). In the present study, we use the latter representation as an acceptable compromise between computational speed and including the appropriate physics.

The other recently added feature in PWOM used in this study is the inclusion of a kinetic treatment of ions (Glocer et al., 2018). Above the ion exobase located at about 2,000 km (Lemaire & Scherer, 1970), the validity of the hydrodynamic approach becomes increasingly suspect as there are few collisions to regularize the distribution function. Moreover, wave-particle interactions such as ion cyclotron heating generate ion conics and other outflow distributions that are far from Maxwellian. PWOM can now treat these nonclassical effects on the global outflow solution using a combined fluid-kinetic approach. Below 1,000 km, PWOM uses its original hydrodynamic approach to solve the gyrotropic transport equations for ions. Above 1,000 km, PWOM uses a hybrid PIC approach with Monte Carlo collisions to obtain a kinetic solution by following guiding center macroparticles for each ion species.

In our simulations where PWOM is coupled to the magnetosphere, we include both electron precipitation and wave-particle interactions. The electron precipitation in this simulation is based on the magnetospheric currents coming into the ionosphere and set according to empirical relationship described by Ridley et al. (2004). The mean energy and energy flux of the precipitation is used to set the electron spectrum at the top of each PWOM field line and in particular sets the upper boundary of each instance of the GLOW code associated with each field line. The associated superthermal electron transport, production, and energy deposition is thus included throughout the high-latitude region as described in our previous studies (Glocer et al., 2017, 2018). For wave-particle interaction, we use the empirical heating terms provided by Barakat and Schunk (2001) in their Equations 3 and 4 for both H^+ and O^+. As done in Glocer et al. (2018), we define a threshold of 1 erg/cm^2/s to determine where to use wave-particle interaction terms appropriate to the cusp and aurora.

Beyond these recent advances, in this study, we now account for separate outflow solutions in each hemisphere. Here we improved on an existing feature of PWOM that has not been often used. We know from observations that the outflow strength and composition have significant seasonal dependence (Lennartsson et al., 2004). However, our past modeling studies have only simulated outflow in the Northern Hemisphere and then assumed the same outflow for the Southern Hemisphere. By including a separate outflow

calculation for each hemisphere, we are now able to study the the role of asymmetric outflow on the magnetosphere.

2.2. Multifluid BATS-R-US

The BATS-R-US code is used to represent the magnetosphere in this paper. BATS-R-US is a truly multiphysics code capable of solving different equation sets in the magnetosphere, including MHD, Hall MHD (Tóth et al., 2008), and anisotropic MHD (Meng et al., 2012). Of particular relevance to this study is the ability to solve the multifluid MHD equations given by Glocer et al. (2009):

$$\frac{\partial \rho_s}{\partial t} + \nabla \cdot \left(\rho_s \mathbf{u}_s\right) = S_{\rho_s} \tag{1}$$

$$\frac{\partial \rho_s \mathbf{u}_s}{\partial t} + \nabla \cdot \left(\rho_s \mathbf{u}_s \mathbf{u}_s + I p_s\right) = n_s q_s \left(\mathbf{u}_s - \mathbf{u}_+\right) \times \mathbf{B} + \frac{n_s q_s}{n_e e} \left(\mathbf{J} \times \mathbf{B} - \nabla p_e\right) + S_{\rho_s \mathbf{u}_s} \tag{2}$$

$$\frac{\partial p_s}{\partial t} + \nabla \cdot \left(p_s \mathbf{u}_s\right) = -\left(\gamma_s - 1\right) p_s \nabla \cdot \mathbf{u}_s + S_{p_s} \tag{3}$$

$$\frac{\partial \mathbf{B}}{\partial t} - \nabla \times \left(\mathbf{u}_+ \times \mathbf{B}\right) = 0 \tag{4}$$

$$\frac{\partial p_e}{\partial t} + \nabla \cdot \left(p_e \mathbf{u}_e\right) = -\left(\gamma_e - 1\right) p_e \nabla \cdot \mathbf{u}_e + S_{p_e} \tag{5}$$

where γ_s is the adiabatic index for ion, and γ_e is the adiabatic index for electrons. The s and e subscripts represent the ion or electron fluids, respectively. Other variables include the ion (q_s) and electron (e) charge densities, the number density (n), mass density (ρ), velocity ($\mathbf{u}$), pressure (p), current density ($\mathbf{J}$), magnetic field ($\mathbf{B}$), and source terms (S), whose subscript indicates the type. $\mathbf{u}_+$ represents the charge-averaged ion velocity defined by the following:

$$\mathbf{u}_+ = \frac{\sum_s n_s q_s \mathbf{u}_s}{e n_e} \tag{6}$$

where n_e is the total electron number density set equal to the sum of the ion number density due to quasineutrality. In these simulations, we set the electron velocity $u_e = u_+$, so the Hall effect is neglected. Note that source term (S_{ρ_s}) representing mass exchange as a result of chemical processes are included here for completeness but are set to zero for this study. On the other hand, a momentum source term ($S_{\rho_s \mathbf{u}_s}$) is included to limit the velocity difference parallel to the magnetic field line and represent the effect of streaming instabilities. This term is described by Glocer et al. (2009) and takes the form of an artificial friction term given by

$$S^{friction}_{\rho \mathbf{u}_s} = \frac{1}{\tau_c} \sum_{q \neq s} \min\left(\rho_s, \rho_q\right)\left(\mathbf{u}_q - \mathbf{u}_s\right)\left(\frac{\left|\mathbf{u}_s - \mathbf{u}_q\right|}{u_c}\right)^{\alpha_c} \tag{7}$$

where q indexes all the other fluids, τ_c is the cut-off time scale, u_c is the cut-off velocity, and α_c is the cut-off exponent. We choose to limit the relative ion velocities parallel to the magnetic field to the local Alfven speed as done in Opher et al. (2020).

In this paper, we advance the multifluid treatment presented in Glocer et al. (2009) in two straightforward but important ways. First, we expand the number of fluids considered to allow for the inclusion of separate H^+ fluids from the high-latitude ionosphere (polar wind) and solar wind as well as a separate plasmasphere fluid. This is an improvement over the treatment in Glocer et al. (2009), which only had two ion fluids (H^+ and O^+). It also builds on the recent work showing the advantages of separating the solar wind and ionospheric H^+ populations. Second, we expanded the coupling between BATS-R-US and CIMI, and BATS-R-US and PWOM, to take advantage of these additional fluids.

2.3. CIMI Model

To model the ring current, we will be using the Comprehensive Inner Magnetosphere-Ionosphere (CIMI) model (Fok et al., 2014). The CIMI model is a kinetic model that combines the Comprehensive Ring Current Model (CRCM) (Fok et al., 2001) and the Radiation Belt Environment (RBE) model (Fok et al., 2011) to obtain energetic ion (0.1–400 keV) and electron (1 keV to 4 MeV) distributions and plasmaspheric densities.

In the version of CIMI coupled with the SWMF, we are solving the bounce-averaged Boltzmann equation for the distribution functions of ring current-radiation belt particles given as follows:

$$\frac{\partial f_s}{\partial t} + \langle \dot{\lambda}_i \rangle \frac{\partial f_s}{\partial \lambda_i} + \langle \dot{\phi}_i \rangle \frac{\partial f_s}{\partial \phi_i} = \frac{1}{G}\frac{\partial}{\partial \alpha_0}\left[G\left(D_{\alpha_0\alpha_0}\frac{\partial f_s}{\partial \alpha_0} + D_{\alpha_0 E}\frac{\partial f_s}{\partial E}\right)\right] + \frac{1}{G}\frac{\partial}{\partial E}\left[G\left(D_{EE}\frac{\partial f_s}{\partial E} + D_{E\alpha_0}\frac{\partial f_s}{\partial \alpha_0}\right)\right] - \nu\sigma_{sH}\langle n_H\rangle f_s - \left(\frac{f_s}{0.5\tau_b}\right)_{losscone} \quad (8)$$

where $G = T(\alpha_0)\sin 2\alpha_0 (E + E_0)\sqrt{E(E + 2E_0)}$. $f_s = f_s(t, \lambda_i, \phi_i, M, K)$ is defined by the average of the distribution function between mirror points of a given field line. The magnetic latitude (λ_i) and local time (ϕ_i) are both defined at the ionospheric foot point of the geomagnetic field line. M is the relativistic magnetic moment, and $K = J/\sqrt{8m_0 M}$, where J is the second adiabatic invariant. Particle motion is described by their drifts across field lines and calculated at ionospheric foot points. The rest energy is given by E_0, and α_0 represents the equatorial pitch angle. $T(\alpha_0)$ is a function depending on α_0 and the shape of the field line.

The left-hand side of Equation 8 represents the drifts of the particle population, while the right-hand side represents source and loss terms due to wave-particle interactions, charge exchange, and the loss cone. The drifts include the gradient-curvature drift, $E \times B$ drift from convection, as well as corotation. Note that the convection electric field is passed to CIMI from the SWMF and represents the electrodynamics coupling between the ionosphere and the magnetosphere. The effects of the inductive electric field due to a time-varying magnetic field are also taken into account implicitly in the model (Keller et al., 2005). In this study, our main focus is on the ring current ions, and thus we ignore VLF wave-particle interactions by setting wave diffusion coefficients in energy (D_{EE}), angle ($D_{\alpha_0\alpha_0}$), and mixed ($D_{\alpha_0 E}$) to zero. They are included here, however, for completeness as they are available in the model. The second to last terms on the right-hand side of Equation 8 represents the charge exchange loss for ions where σ_{sH} is the charge exchange cross section for a species "s" with hydrogen in the geocorona. The final term on the right-hand side of Equation 8 represents the loss cone loss with a half bounce period lifetime.

Critical to the the present study is the inclusion of a separate plasmasphere fluid in the multifluid BATS-R-US code. That fluid is filled entirely from the CIMI code based on its embedded core plasmasphere model. That model solves an equation for the total plasmasphere ion content (N) per unit magnetic flux according the following equation:

$$\frac{\partial N}{\partial t} + \langle \dot{\lambda}_i \rangle \frac{\partial N}{\partial \lambda_i} + \langle \dot{\phi}_i \rangle \frac{\partial N}{\partial \phi_i} = \frac{F_n + F_s}{B_i} \quad (9)$$

where F_N and F_S are empirical refilling rates for the Northern and Southern Hemispheres. The plasmasphere model calculates plasmaspheric density distribution considering corotation, convection, daytime refilling, and nightside diffusion (Fok et al., 2005). These densities are then fed back to BATS-R-US to populate the plasmasphere fluid with two important assumptions. First, this type of plasmasphere model does not have information regarding the density distribution along the field line. We therefore make the simplest assumption that the average density is constant along the field line. Second, this type of plasmasphere model does not specify the plasmasphere temperature or pressure. We therefore assume a temperature of 1 eV and then hold the pressure fixed along the field line. These assumptions can be relaxed in the future as new plasmasphere representations become available in CIMI, but they suffice for the present study.

3. Case Study: The 6–7 June 2013 Event

In this paper, we aim to illustrate the importance of three issues: (1) the relative importance of solar wind and ionospheric protons, (2) the impact of hemispheric asymmetry of outflow on magnetospheric composition, and (3) the impact of the plasmasphere on the global magnetospheric solution. To that end, we apply our model described in the previous section to the particular event of 6–7 June 2013. This is a modest event with a maximum Kp index of 6 and minimum Dst of −78 nT. The F10.7 value of 110 indicates that the solar EUV flux input is also modest, although there is a significant seasonal asymmetry in illumination. The solar wind conditions upstream of the magnetosphere are given in Figure 1. Our simulation time goes from just before the large southward Bz turning on 6 June and runs for approximately 1 day. In order to examine the effect of the plasmasphere, we conduct this simulation both with a very full plasmasphere and without any plasmasphere. These two cases represent limiting scenarios that enable us to examine the maximum extent

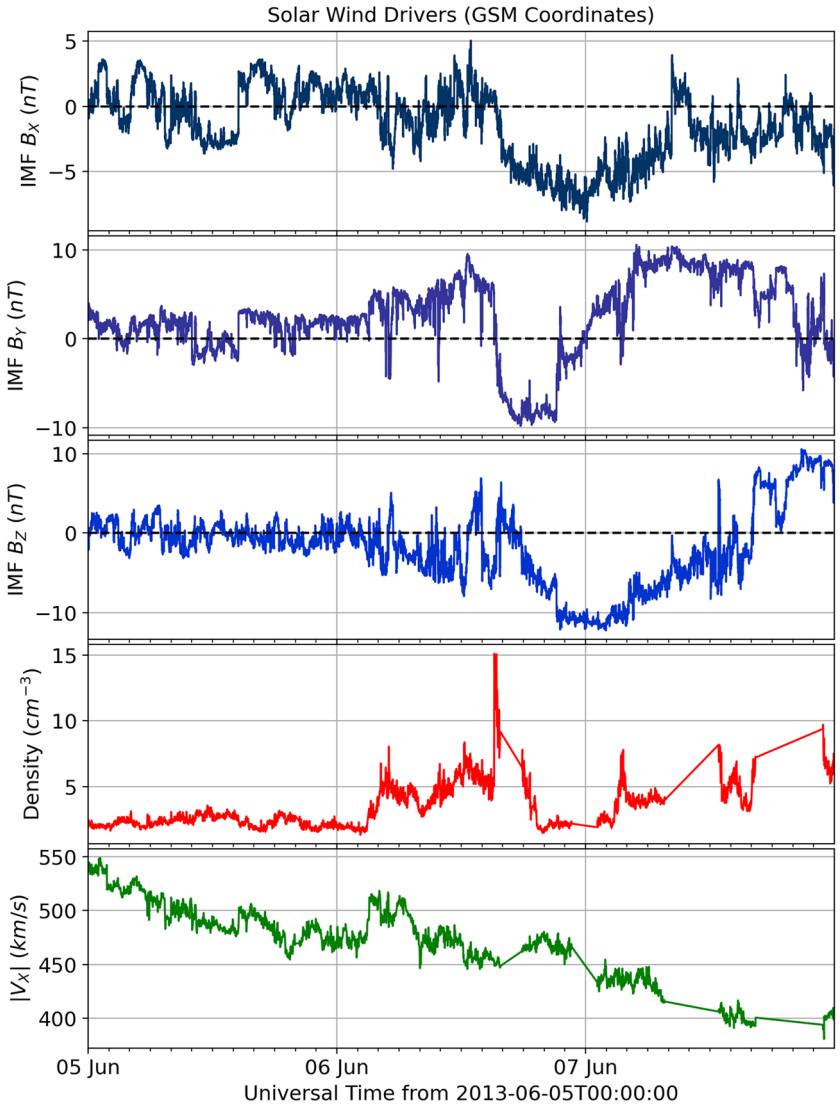

Figure 1. Solar wind conditions during the 6–7 June 2013 event from the ACE satellite.

of plasmaspheric impacts on the system. In each case, we are able separate the relative contribution of O^+ as well as solar wind and ionospheric protons to the magnetosphere and into the ring current.

We begin our analysis by examining the outflow solution during the storm. Figure 2 shows a map of the outflow fluxes of O^+ and H^+ during the main phase of the event for both the Northern and Southern Hemispheres. Each panel is a slice at a constant altitude of 6,000 km with the sunward direction toward the top of the plot. The locations of the field-line foot-points in the simulation at this time are indicated by the white '+' symbols. The overall outflow flux for both H^+ and O^+ is stronger in the northern summer hemisphere and weaker in the southern winter hemisphere. However, the effect is more strongly seen in the O^+ flux that exhibits a much stronger seasonal dependence. We find that the H^+ flux is generally spread out over the sunlit high latitude region, which covers a larger portion of the Northern Hemisphere than the Southern Hemisphere. The O^+ flux, in contrast, is organized more around the auroral zone and cusp. Additionally, there is a pronounced dawnward shift from noon of the O^+ flux at this time. At later times in the event (not shown), the shift becomes less obvious or even disappears. As discussed by Redmon et al. (2012), observations indicate that a dawnward shift in the peak dayside O^+ flux is expected during low activity periods, but the shift can disappear during active times.

In terms of the overall fluxes, we note that the values shown are reasonable as compared to observations. In Figure 2, we find the H^+ fluxes to be on the order of 10^7 $cm^{-2}s^{-1}$ at 6,000 km. That value corresponds well

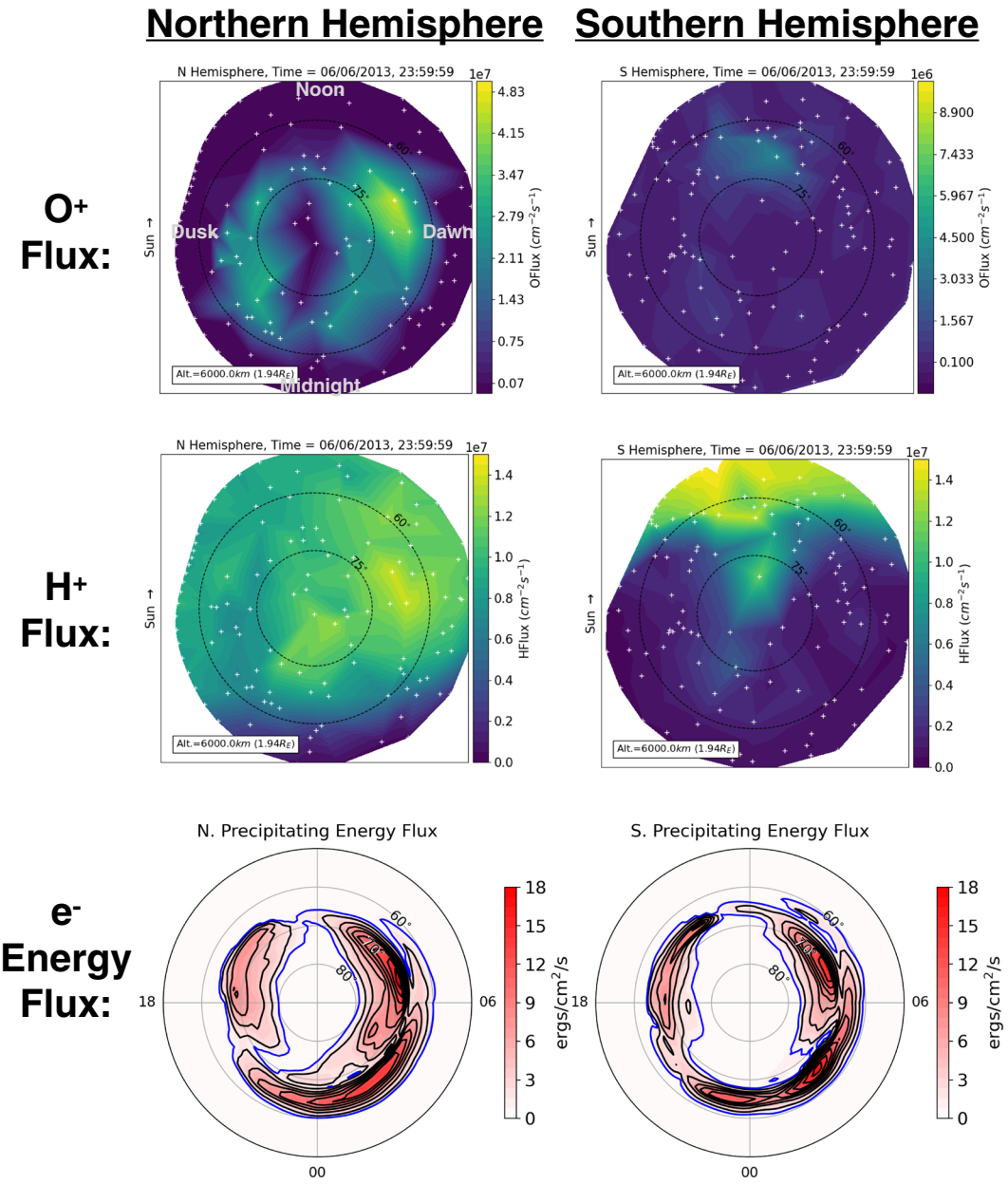

Figure 2. The outflowing ion fluxes during the main phase of the storm illustrating the hemispheric asymmetry of the outflow. The Northern (left column) and Southern (right column) Hemispheres are shown for O^+ (top row) and H^+ (middle row). Note that the O^+ flux in the Southern Hemisphere has the peak of the color bar reduced by approximately a factor of 5 to compensate for the much weaker outflow. The case without plasmasphere is shown. The white "+" symbols denote the location of the field-line foot points in the simulation. The bottom row shows the electron precipitating energy flux at this time at an altitude of 110 km. The blue contour corresponds to 1 erg/cm^2/s. All latitudes in this figure are invariant latitudes.

with observed values of the polar wind. For instance, Hoffman and Dodson (1980) reported observations of polar wind fluxes from the Isis 2 satellite on the order of 10^8 cm^{-2}s^{-1} at 1,400 km, which corresponds to a flux of about 2.5×10^7 cm^{-2}s^{-1} at 6,000 km. Similar values of 6.0×10^7 cm^{-2}s^{-1} at 5,000 km are reported by Huddleston et al. (2005) from Polar spacecraft observations. Therefore, our modeled H^+ fluxes are on the same order, if somewhat less than observed levels. In contrast, it is harder to estimate the reasonableness of the O^+ fluxes whose observations have shown to be highly variable and depend strongly on the energization. Indeed, observations from the Fast Auroral SnapshoT (FAST) satellite shows accelerated O^+ fluxes anywhere between 10^5 and 10^9 cm^{-2}s^{-1} at about 4,000 km (Strangeway et al., 2005; Zhao et al., 2020). Our peak fluxes,

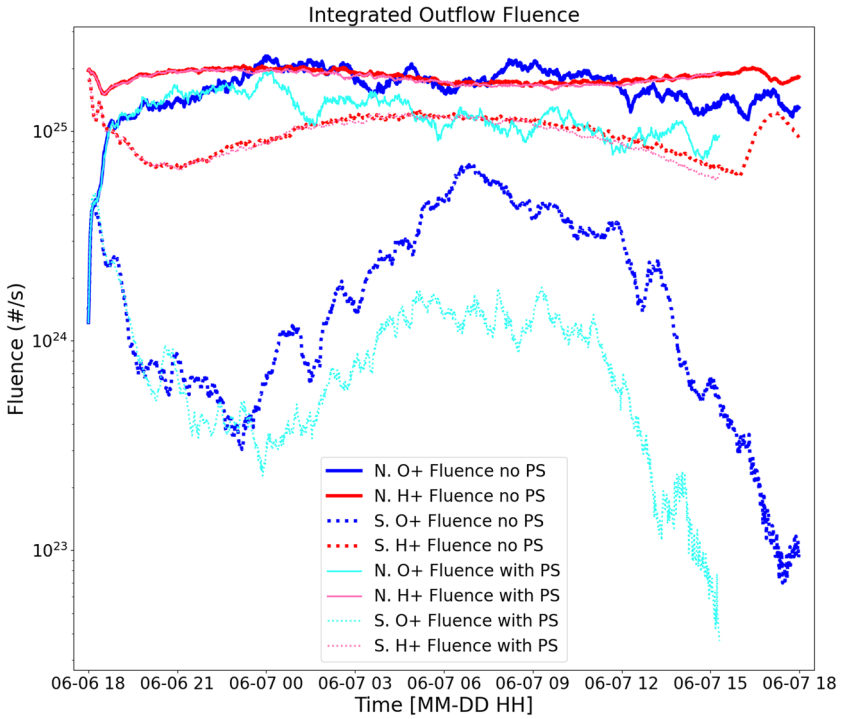

Figure 3. The integrated fluence of O^+ (blue/cyan line) and H^+ (red/pink line) particles coming out of the Northern (solid line) and Southern (dotted line) Hemispheres. The solution is shown both without (thick line) and with (thin line) an included plasmasphere. We see stronger outflow in the northern summer hemisphere and that the inclusion of a plasmasphere suppresses the O^+ outflow.

on the order of 4.0×10^7 cm^{-2}s^{-1}, fall within the range of past observations, but no stronger claim can be made without more available data.

It also is interesting to evaluate the role of asymmetry in the precipitation as a possible contributor to the asymmetry in the outflow flux. We therefore include the precipitating electron energy flux in each hemisphere in the bottom row of Figure 2. While there are modest differences in the precipitation patterns between the Northern and Southern Hemispheres, the two precipitating distributions are qualitatively similar. Moreover, as the wave-particle interactions in the auroral region are applied in the model by evaluating when the energy flux crosses a threshold of 1 erg/cm^2/s (see section 2.1) as indicated by the blue contour line, comparable wave-heating is specified in each hemisphere. As a result, we do not believe asymmetric auroral precipitation has a significant contribution to the hemispheric asymmetry of the outflow in our simulation.

To make the outflow solution more quantitative, we calculate the net fluence, defined by the number of particles coming out of each hemisphere at each time in our simulations. To compute this value, we extract the solution each minute at 6,000 km that is near the top of the simulation domain. That extracted solution is on an unstructured grid defined by the field-line locations at each time. We interpolate the solution from the unstructured grid onto a regular spherical grid and integrate the number flux times the area element to obtain fluence for O^+ and H^+ at each time.

Figure 3 presents the net fluences of O^+ and H^+ particles coming out of each hemisphere for simulations with and without a plasmasphere included. Similar to the results shown in Figure 2, we see a strong seasonal asymmetry in the outflow solution with more H^+ and O^+ outflow in the northern summer hemisphere and less in the southern winter hemisphere. Additionally, the seasonal asymmetry is more pronounced for O^+ than for H^+. Figure 3 further demonstrates that the inclusion of a plasmasphere in the magnetospheric solution suppresses the O^+ outflow and changes the composition of the total outflow. Specifically, when a plasmasphere is included, the fluence O^+ decreases and the outflow composition contains a higher proportion of H^+ and a lower proportion of O^+. Possible reasons for this plasmaspheric impact will be discussed later.

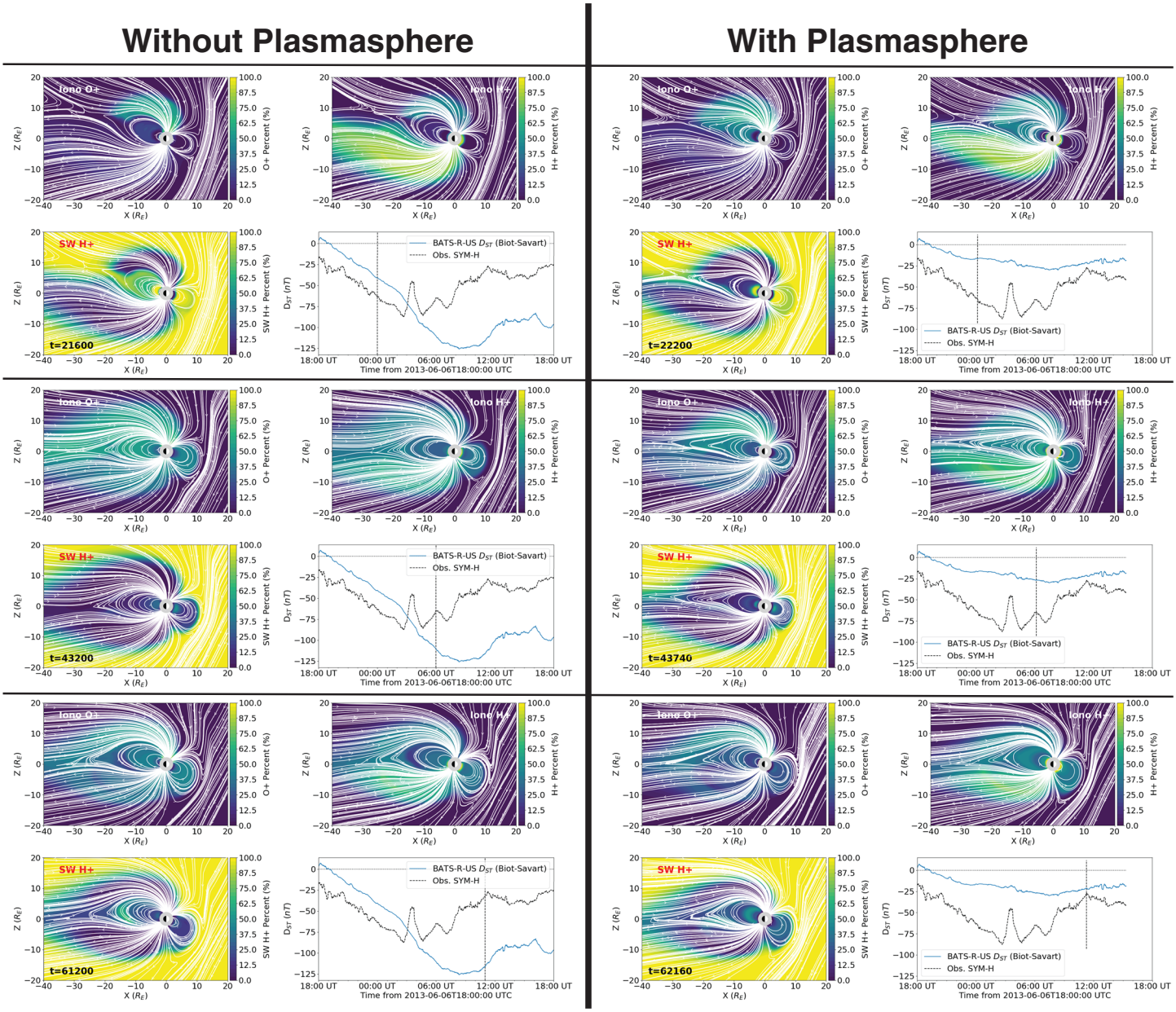

Figure 4. The evolution of the magnetospheric composition without plasmasphere (left column) and with plasmasphere (right column). Each panel has three color contour plots in the $y = 0$ GSM plane showing the percentage of plasma from each source, excluding the plasmasphere fluid. Each panel also has a comparison of the simulated Dst with observations, with vertical dashed line indicating the time shown in the panel.

The hemispheric asymmetry seen in the outflow solution is manifest in the magnetosphere. Figure 4 presents the evolution of magnetospheric composition with and without plasmasphere. Three time periods are shown: the storm main phase, the storm peak, and during the early recovery. Each panel of the figure shows $y = 0$ GSM plane at a particular time, with color contours representing the percentage of plasma contributed by each constituent species. These include ionospheric O^+ and H^+ as well as solar wind H^+. Note that for this comparison, we do not include the plasmasphere fluid in the percentage calculation. We find that in both simulations, the asymmetry in the outflow solution translates into asymmetric composition in the lobes. Specifically, we find that the northern lobe has a higher percentage of O^+ than the southern lobe, and the southern lobe is mostly populated by polar wind protons. Interestingly, composition asymmetry can at times persist all the way to the x-line in the tail, resulting in asymmetry in composition on either side of the x-line.

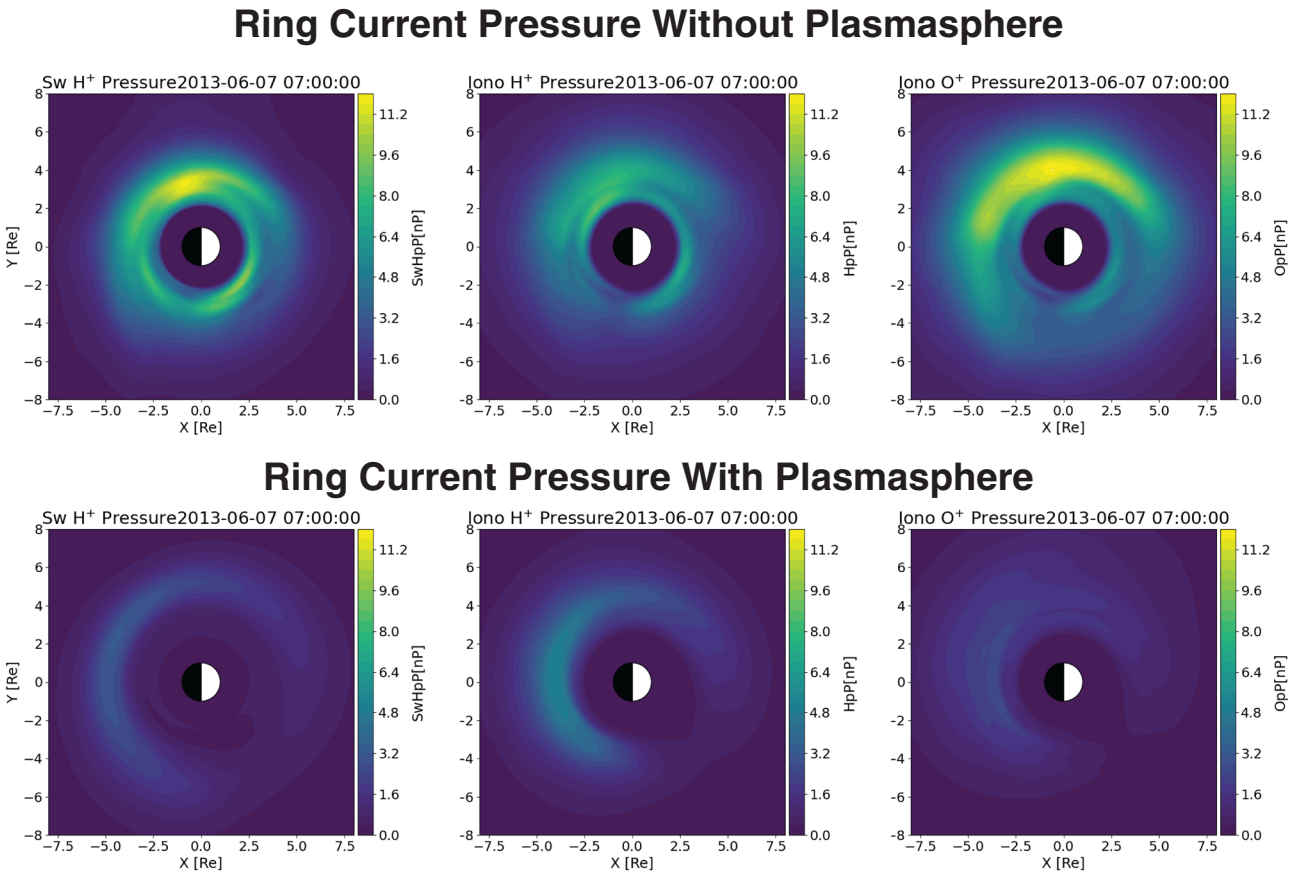

Figure 5. The ring current pressure near the peak of the storm for solar wind H^+ (left), ionospheric H^+, and ionospheric O^+. Results are shown without a plasmasphere included (top) and with a plasmasphere included (bottom).

The evolution of the magnetosphere from one whose plasma mostly comes from the solar wind to one whose plasma mostly comes from the ionosphere is also evident in Figure 4. Our simulation starts with only solar wind plasma, but during the main phase of the storm, much of the solar wind is flushed out of the plasmasheet and is largely replaced with ionospheric H^+ and O^+. This change in composition is substantial but not permanent. During the early recovery, additional solar wind H^+ gets reinjected into the plasmasheet, and solar wind protons begin to slowly reestablish their contribution to the plasmasheet. While the story is largely similar regardless of whether plasmasphere is included or not, there are some differences. For example, the solar wind protons get displaced more rapidly when the plasmasphere is included, and the calculated Dst index is much lower without the plasmasphere, indicating a more intense ring current. Both effects are likely due to a reduction of efficiency in the solar wind-magnetosphere coupling when a plasmasphere is included, which will be further discussed later in this section.

Moving inward from the plasmasheet, we shift our focus to the ring current solution. Figure 5 presents the ring current pressure from the CIMI model on the surface defined by the minimum of the magnetic field at a time near the storm peak. Pressure values are shown for solar wind and ionospheric protons as well as ionospheric O^+. We find that the ring current pressure in each species is strongly reduced when the plasmasphere is included. In the case when no plasmasphere is included, the O^+ is the dominant contributor to the pressure, followed by the solar wind protons and then protons of ionospheric origin. Additionally, multiple ring current injections occur when examining a time series of simulation output (not shown). When including the plasmasphere, the ring current is less dynamic with fewer injections. Moreover, H^+ of ionospheric origin is found to be the largest contributor to the ring current pressure at this time.

To understand how different plasma sources contribute to the ring current over time, it is useful to examine the total ring current energy carried by each constituent. We do this by integrating over phase space at each time to obtain the total energy carried by solar wind H^+, ionospheric H^+, and ionospheric O^+.

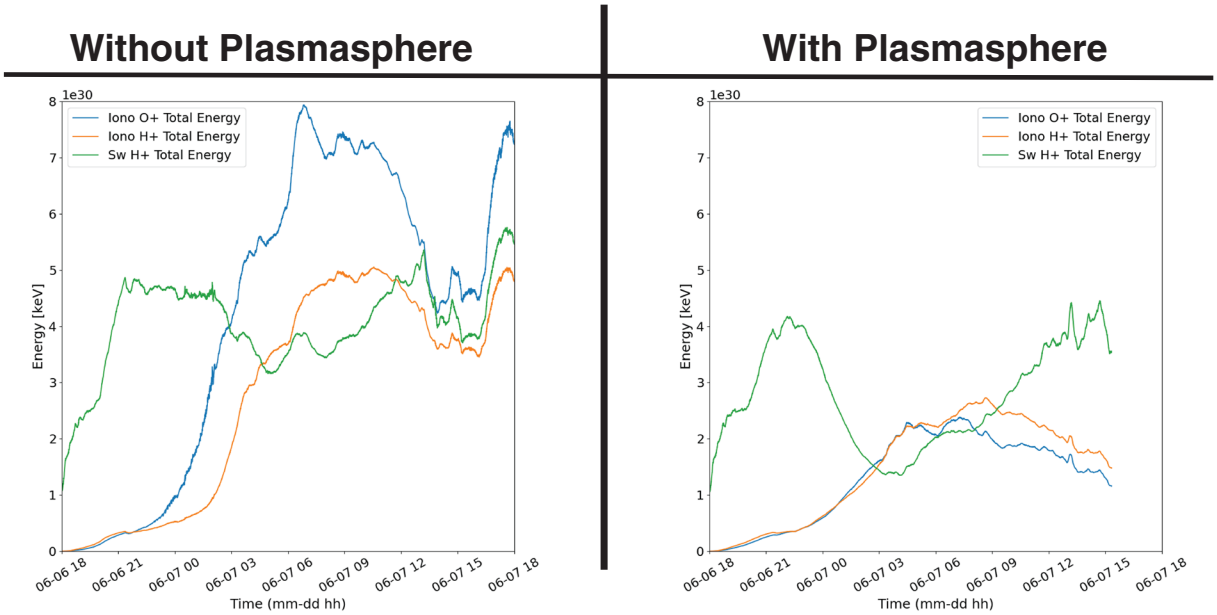

Figure 6. Total energy content in the ring current by species as a function of time when a plasmasphere is not included (left) and when a plasmasphere is included (right).

That time series is presented in Figure 6. When the plasmasphere is not included, O^+ carries most of the energy density from the peak of the storm until the end of the simulation. The solar wind and ionospheric H^+ become roughly equal contributors to the ring current energy during this period. When the plasmasphere is included, the overall energy in the ring current in sharply reduced. During the peak of the storm, the ionosphere briefly becomes the main contributor to the ring current plasma, but later in the simulation, the solar wind and ionospheric contributions become roughly equal (summing ionospheric species together). Interestingly, if one were to assume that all protons came from the solar wind, as is often the case, then in both simulations, the solar wind would be the dominant contributor to the ring current energy. However, by separating the solar wind and ionospheric protons into two populations, it is clear that the ionosphere contributes a major portion of the ring current in both simulations for this fairly moderate event.

Thus far, in this section, we have found that the plasmasphere as we have modeled it can have a profound impact on the entire magnetosphere. Our hypothesis for this effect is that the initially very full plasmasphere forms a drainage plume during the storm main phase that then creates a region of very high density at the dayside magnetopause. Cold dense plasma near the reconnection site drives the dayside reconnection rate down as indicated by prior studies (Borovsky & Steinberg, 2006; Ouellette et al., 2016; Walsh et al., 2014). As the reconnection rate is reduced, the effectiveness of the transfer of energy from the solar wind to the magnetosphere is also decreased. The reduction in the coupling efficiency has a system-wide effect. It reduces the outflow and changes the composition of the ionospheric plasma entering the magnetosphere, slows the convection in the magnetotail, reduces the build up of the ring current, and impacts magnetospheric composition. This is the first time such a system-wide impact due to the plasmasphere has been demonstrated in either simulation or observations.

To test our hypothesis, we examine the location of the density increase at the dayside magnetopause relative to the reconnection separator line, and then the impact on solar wind-magnetosphere coupling. Figure 7 shows a 3-D representation of the plasmasphere using isosurfaces of constant density. The figure also shows the open-closed field line boundary with the total mass density painted on the surface and the magnetic separator extracted using the technique described in Glocer et al. (2016). The density on the dayside magnetopause is strongly enhanced in the vicinity of the separator, the line along which reconnection is occurring. We note that the density of the plume near the magnetopause, on the order of 10 cm^{-3}, is reasonable compared with typical spacecraft observations of plasmaspheric drainage plumes (e.g., Lee & Angelopoulos, 2014; Lee et al., 2016; Walsh et al., 2013). It is also interesting to note that the separator exhibits a twist at the

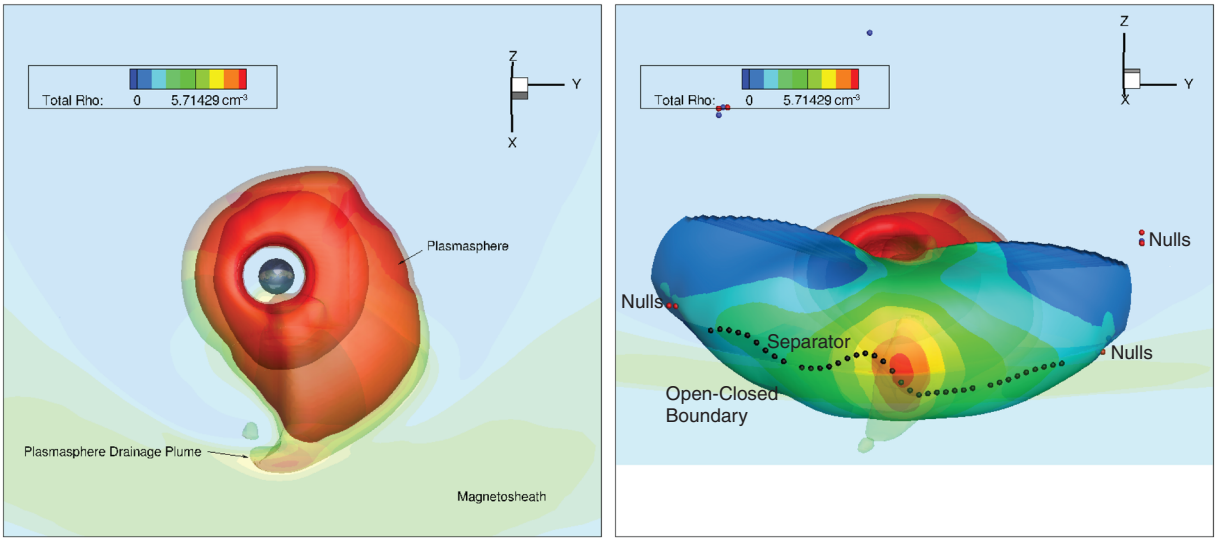

Figure 7. 3-D representation of the plasmasphere plume (shown as isosurfaces), encountering the open-closed field line boundary. Two perspectives are shown: top down and upstream of the magnetosphere. The magnetic separator is indicated by the black dots and the nulls by the colored dots. The time is 4 hr into the simulation or about 30 min after the initial plume arrival at the magnetopause.

location that the plume encounters the magnetopause. The enhanced density at the separator is expected to reduce the reconnection rate and the convection in the magnetosphere.

Evidence of the reduced coupling of the solar wind energy into the magnetosphere is found when looking at the cross polar cap potential. Figure 8 compares the cross polar cap potential in the Northern Hemisphere for cases without and with a plasmasphere included. The approximate arrival time of the plume at the magnetopause is indicated by the vertical dashed line in the plot. Prior to the plume arrival at the magnetopause, the two simulations are remarkably similar. However, after the plume arrival, the two solutions begin to diverge significantly. The simulation with a plasmasphere exhibits a lower cross polar cap potential than the simulation without a plasmasphere. The reduced polar cap potential is indicative of reduced energy input to the magnetosphere, which is likely the cause of the reduced convection and other systematic changes seen in our simulations.

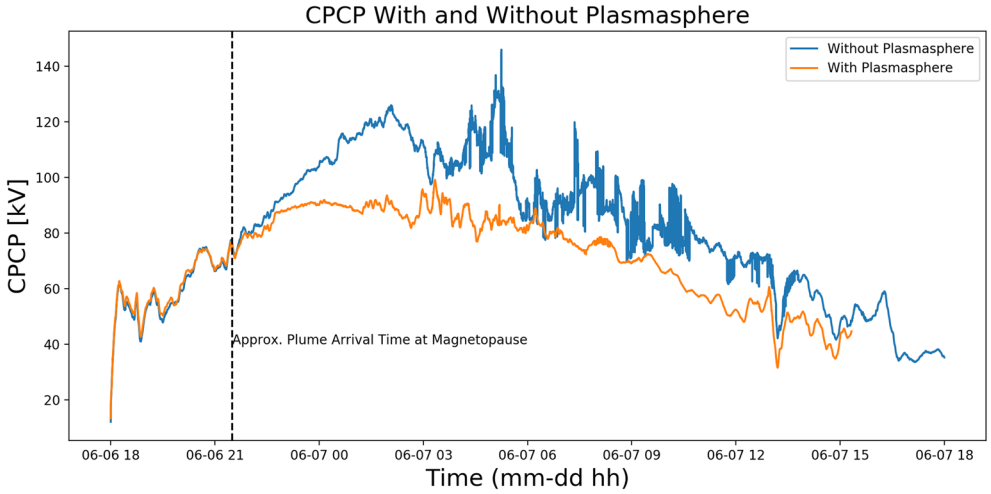

Figure 8. The temporal evolution of the cross polar cap potential (CPCP) in the Northern Hemisphere without (blue) and with (orange) a plasmasphere included. Note that the plume arrives at the magnetopause approximately 3.5 hr into the simulation.

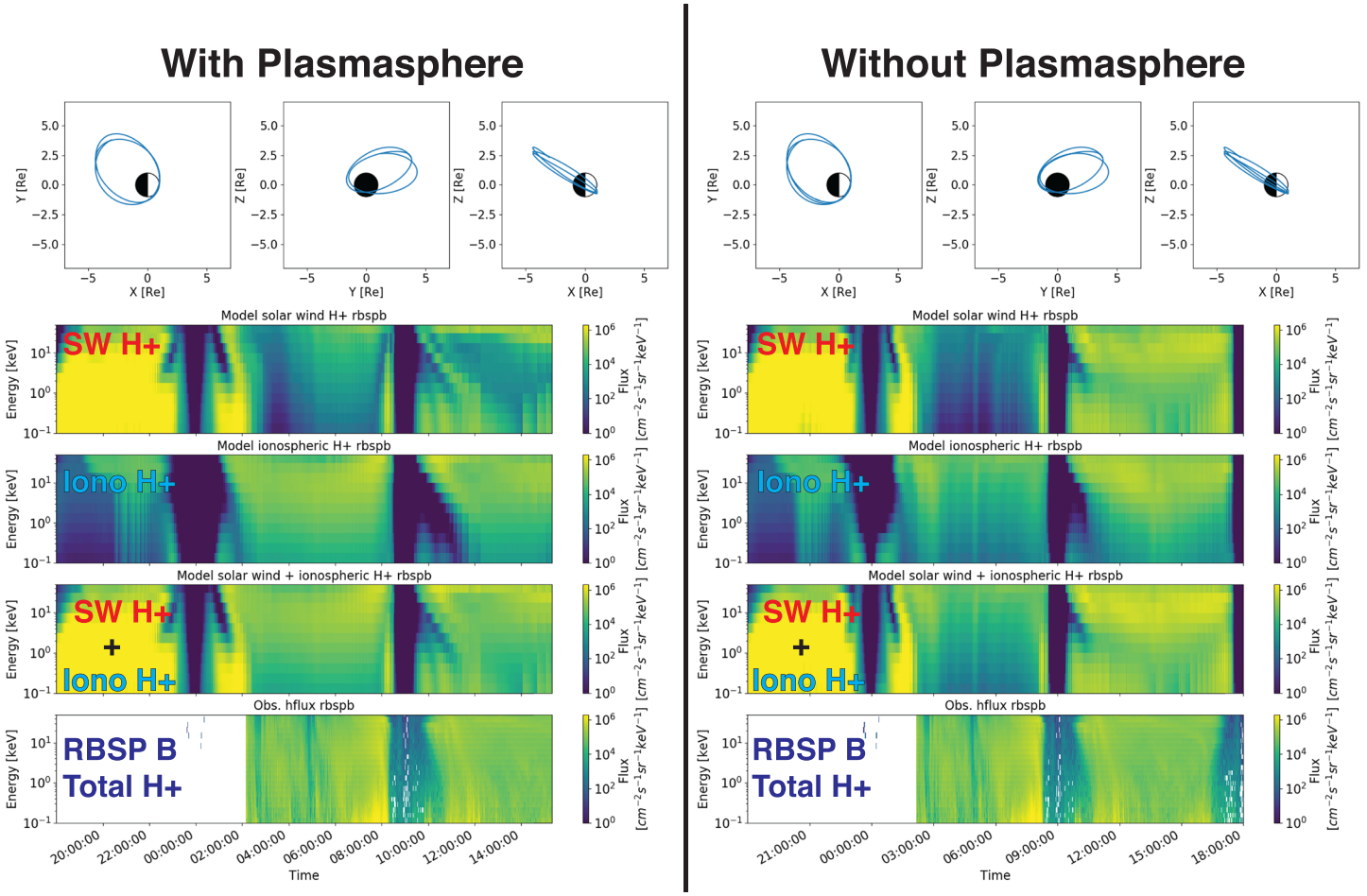

Figure 9. Comparison of simulated and observed H^+ ion spectra along the RBSP B satellite trajectory starting on 6 June and ending on 7 June. The orbit is shown in the top panel, the first and second rows of spectra represent the simulated solar wind and ionospheric H^+, respectively. The third row of spectra presents the total solar wind and ionospheric H^+. The total observed H^+ is shown on the bottom. The simulation with plasmasphere is on the left, and the simulation without plasmasphere is on the right.

4. Comparison With Van Allen Probe Data

In the prior section, we found a number of interesting features in the simulation in terms of the relative contribution of different sources of plasma, the role of hemispheric asymmetry of outflow, and the system-wide impact of including the plasmasphere. However, the only data-model comparison included thus far has been with the Dst index, which is a good overall measure of ring current intensity but lacks composition information. Fortunately, Van Allen Probe (RBSP) data of ion composition from the HOPE instrument is available from the peak of the storm onward. While perfectly fitting the observations is not an objective of this study, comparison with the observations can yield some guidance on the overall reasonableness of the simulations.

Figure 9 presents the comparison of the simulated and observed proton spectra along the RBSP B satellite trajectory. As RBSP A and B are in very similar orbits at this time, we only present the comparison with one satellite and simply note that similar results are found for each satellite. We extract synthetic spectra of solar wind and ionospheric H^+ from the CIMI portion of the coupled model using the technique described in Glocer et al. (2013). Those results are compared with the observed proton spectra from HOPE, which necessarily represents the total proton solution from every source. From the comparison of the simulated and observed spectra, we note the following. First, we find that at the peak of the storm, protons of ionospheric origin are able to account for much of the observed protons in the HOPE energy range. But toward the end of the simulation, both ionospheric and solar wind proton sources become important again. Second, the overall intensity of the observed and simulated spectra are comparable, and some similarity of features is evident, indicating a qualitative agreement. Moreover, summing up the solar wind and ionospheric protons gives

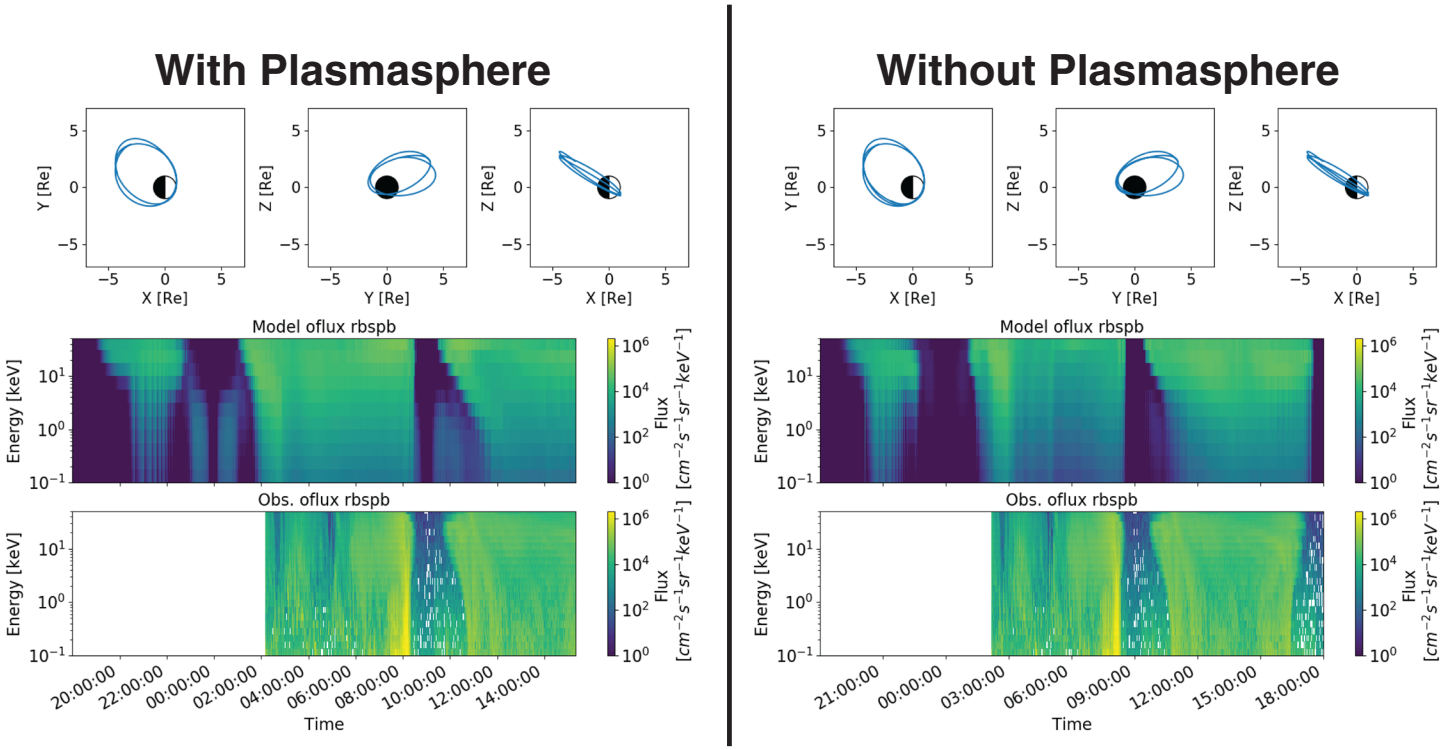

Figure 10. Comparison of simulated and observed O^+ ion spectra along the RBSP B satellite trajectory starting on 6 June and ending on 7 June. The orbit is shown in the top panel, the top spectra represent the ionospheric O^+. The observed O^+ is shown on the bottom. The simulation with plasmasphere is on the left, and the simulation without plasmasphere is on the right.

a better qualitative comparison to the observations, indicating that both sources of protons are required to adequately understand protons in the ring current. Finally, we note that the simulation with plasmasphere has protons of ionospheric origin playing a somewhat more prominent role as compared to the simulation without a plasmasphere included. This is consistent with our analysis of the ring current energy in the previous section that found ionospheric H^+ carries more ring current pressure in the simulation when a plasmasphere is included.

Figure 10 presents the comparison of the simulated and observed O^+ spectra along the RBSP B satellite trajectory. Again, the overall intensity of the simulated and observed spectra are similar as are some of the features, indicating a qualitative agreement. We note that when the plasmasphere is included, there appears to be more O^+ in the simulated HOPE energy range as the simulation without a plasmasphere has a hotter population shifting part of the flux to higher energies. Additionally, the simulation with a plasmasphere appears smoother near the peak of the storm (3–7 UT) than the case without a plasmasphere, consistent with this simulation showing fewer O^+ injections.

Clearly, there is a strong difference seen when including a plasmasphere, but it is important to note that we are focusing on two limiting cases: no plasmasphere and very full plasmasphere. No attempt was made to initialize with the observed values. Instead, we use these limiting cases to establish the impact the plasmasphere may have on the system. Comparison of the simulated plasmasphere with the observed total electron density from EMFISIS (not shown) indicates reasonable agreement inside of the plasmapause but that the simulated plasmapause extends further out than is observed. This is entirely due to the initial condition and is intentional.

5. Discussion and Conclusions

In this study, we focused on three issues: the relative contribution of ionospheric and solar wind protons during a storm, the hemispheric asymmetry of outflow and its consequences for the magnetosphere, and the system-wide impact of the plasmasphere. To enable this study, we use the SWMF to couple models of ionospheric outflow (PWOM), the global magnetosphere (BATS-R-US), the ionosphere electrodynamics,

and an embedded inner magnetosphere model (CIMI) as described by Glocer et al. (2018) with some key improvements, including the option of including a plasmasphere model. For the remainder of this section, we will summarize and discuss the modeling advancements and scientific findings of our study.

The key modeling enhancements we introduce relative to the model described in Glocer et al. (2018) include adding the ability to separately track ionospheric and solar wind protons in the magnetosphere (building on recent work), including separate outflow representations for each hemisphere, and including a separate cold plasmasphere fluid in the magnetosphere. While new to our modeling studies, the first two features are present to some degree in previous studies. For instance, separation of solar wind and ionospheric protons was included in the test particle modes like Moore et al. (2005) but without a first principles model of ion outflow. The separation of proton sources is also included in the fluid model of Varney et al. (2016) but without separate Northern and Southern Hemisphere ion outflow solutions. Similarly, hemispheric asymmetries of outflow are examined in the first principles outflow model of Schunk and Sojka (1997), but no coupling of the outflow into the magnetosphere is included. The present model represents a tangible step forward in that it includes a first principles model of ionospheric outflow coupled to the magnetosphere, with hemispheric asymmetry, and separate fluids for the solar wind and ionospheric protons.

Including cold plasmasphere and hot ring current populations simultaneously in a global magnetosphere model is likewise a significant advance. When a typical single-fluid global magnetosphere model is coupled to an inner magnetosphere model (e.g., De Zeeuw et al., 2004; Glocer et al., 2013; Meng et al., 2013), a choice typically has to be made as to whether to represent the plasmasphere, which carries the majority of the density, or the ring current, which carries the pressure. This is because the distribution function underpinning a typical single-fluid MHD model cannot simultaneously represent the cold and hot populations simultaneously. The advent of multifluid magnetospheric models, however, makes it possible to couple the hot and cold populations to separate fluids. Nevertheless, until now, multifluid codes have either included a plasmasphere without a ring current model (e.g., Ouellette et al., 2016; Zhang et al., 2016) or a ring current without a plasmasphere (Glocer et al., 2018). In the present work, we allow an inner magnetosphere model, CIMI, to advance the ring current and plasmasphere solutions in the inner magnetosphere while fully coupled to the multifluid BATS-R-US magnetosphere model. In this way, a multicomponent hot ring current and cold plasmasphere can be included simultaneously in the global magnetosphere for the first time.

When the modeling advances described above were applied to the geomagnetic storm of 6–7 June 2013, we found that ionospheric protons play a major role in populating the magnetosphere. During the storm main phase and peak, protons of ionospheric origin make up a major portion of the plasmasheet, displacing much of the solar wind proton contribution. Similarly, ionospheric protons comprise a significant portion of the ring current pressure during this time. Later in the simulation, solar wind protons start to build up again in the plasmasheet and ring current due to new injections from the tail. Just how much the ionospheric protons contribute to the ring current and plasmasheet depends on the simulation (with or with plasmasphere), but in either case, their contribution cannot be ignored. These results are consistent with the past work of Huddleston et al. (2005), who combined estimates of the polar wind proton fluxes with particle tracing in empirical magnetic fields. They demonstrated that initially cold outflow can get energized in the magnetotail and be a major contributor to the plasmasheet and ring current. Indeed, we similarly have cold outflow that gets energized in the magnetosphere to build the plasmasheet and ring current.

It is particularly important to note that ionospheric protons supply cold protons to the magnetosphere that do not remain cold. It is commonly assumed that ionospheric protons do not make up a significant portion of the plasmasheet or ring current because they are simply at too low an energy. However, O^+ that comes out at similarly cold temperatures is observed to be accelerated to tens of keV in the ring current and is also observed to be heated in other parts of the magnetosphere. There is no reason that ionospheric H^+ cannot be similarly accelerated. Moreover, the polar wind is constantly supplying protons directly to the magnetosphere, unlike the solar wind protons that have to enter through reconnection or or other magnetopause interactions. It should therefore be the expectation, rather than the exception, that ionospheric protons are significant contributors to warm and hot populations in the magnetosphere.

As an illustration of this last point, in Figure 11, we demonstrate the heating that an initially cold ionospheric H^+ particle can undergo in the magnetosphere. In this figure, we follow "particles" moving along with the ionospheric H^+ fluid velocity near 5UT launched from a location above the dayside MHD inner boundary. These are not true particles as they follow the bulk fluid velocity, but can be rather thought of

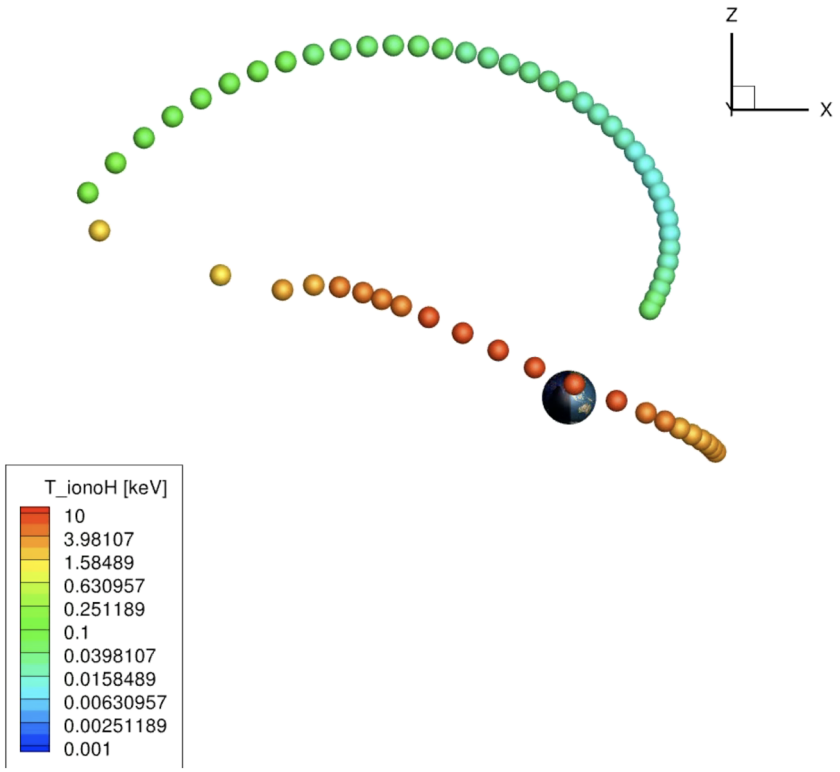

Figure 11. In this figure, we show "particles" following the ionospheric H^+ fluid velocity near 5 UT. The particles are launched above the MHD inner boundary and flow back to the tail where they are brought earthward by the cross tail convection electric field. The particles are colored by the the ionospheric H^+ temperature showing how the initially cold ionospheric population is accelerated to plasmasheet and warm plasma cloak temperatures.

as corks dropped in the river and picked up by the current. The surface of each particle is painted with a color indicating the ionospheric H^+ temperature, thus illustrating how the temperature changes as parcel of plasma travels through the magnetosphere. We find that ionospheric H^+ at the start of the trace near the inner boundary is around 10 eV. As you follow the path of particles out into the lobes to the magnetotail, the temperature grows to nearly 100 eV. When the ionospheric H^+ hits the tail and starts to convect inward due to the cross tail electric field, the temperature rapidly increases to 1–2 keV and then to 4–7 keV. Note that the transition from 100 eV to 1–2 keV is very fast once the plasma feels the cross tail electric field and happens within a few Earth radii. The now-heated ionospheric H^+ contributes to the formation of the plasmasheet and warm plasma cloak (Chappell et al., 2008). Only one trajectory is analyzed here to illustrate the point, but other trajectories tell a similar story. These results corroborate the picture put forward by Huddleston et al. (2005), who followed similar trajectories illustrating how cold ionospheric H^+ is heated.

In our simulations, we also found significant hemispheric asymmetry of outflow with important consequences for magnetospheric composition. In particular, we found that the outflow was stronger in the northern summer hemisphere and weaker in the southern winter hemisphere. We also found that the O^+ exhibited a much stronger seasonal variation than H^+. This result is qualitatively consistent with the observed seasonal asymmetry in a study using Polar data (Lennartsson et al., 2004). Asymmetric outflow is further found to fill the magnetospheric lobes asymmetrically with the northern lobe receiving more ionospheric plasma with a higher proportion of O^+ and the southern lobe receiving less ionospheric plasma with a higher proportion of H^+. Although not studied here, we expect this asymmetric lobe filling to have consequences for reconnection in the tail. For example, asymmetries in outflow are suggested to result in flapping of the magnetotail (Barakat et al., 2015). Beyond this, we speculate that asymmetric lobe filling can be expected to create asymmetric O^+ density conditions near the nightside reconnection site. Recent work by Kolstø et al. (2020) using PIC simulations indicate that such conditions can cause asymmetries in the diffusion region and motion of the reconnection site.

The final focus of our simulation was on the potential consequences of the plasmasphere on the broader geospace system. We found that when the plasmasphere encounters the dayside magnetopause, the global reconnection rate decreases as indicated by the cross polar cap potential. This is consistent with expectations from prior studies (Borovsky & Steinberg, 2006; Ouellette et al., 2016; Walsh et al., 2014). Beyond these past studies, we were able to demonstrate a system-wide impact as the diminished reconnection rate reduced the effectiveness of the solar wind–magnetosphere coupling. This resulted in reduced outflow leaving the ionosphere, a different composition of outflow leaving the ionosphere, changes in the plasma sheet composition, and changes in the ring current intensity and composition. These changes are found to begin shortly after the plume's arrival at the magnetopause where it raises the density near the reconnection separator and, interestingly, causes the separator to twist locally. The timing of these system level impacts is an interesting topic worthy of future investigation. For now, we only note that the earliest effect in the reduction of the O^+ fluence occurs about 30 min after the plume arrival at the magnetopause and becomes sustained after about 2.5 hr. It is important to note that the plasmasphere, which is extremely cold and by itself carries very little energy density, can cause broad changes to the magnetosphere including the relative supply of plasma and the intensity of the warm and hot constituents. This result implies that the preconditioning of the plasmasphere may be important for storm strength and progression. To our knowledge, this is the first time such a far reaching system-wide impact of the plasmasphere has been demonstrated in either data or simulations.

In conclusion, our simulations indicate that the ionosphere cannot be neglected as a source of plasma when trying to understand geomagnetic storms. This is true for high-latitude outflow as well as low-latitude outflow that forms the plasmasphere. Additionally, it is improper to assume that all protons in the magnetosphere come from the solar wind. Our study, however, is only for one fairly modest geomagnetic event, and future work is required to understand how well these conclusions hold for storms of different intensities and with different solar ionizing fluxes.

Data Availability Statement

Resources supporting this work were provided by the NASA High-End Computing (HEC) Program through the NASA Advanced Supercomputing (NAS) Division at Ames Research Center. All modeling tools described in publication are available online through the University of Michigan for download with the SWMF. The model output data used in production of all figures have been made available online for download at http://doi.org/10.5281/zenodo.3767201. We acknowledge the HOPE instrument team for making all RBSP-ECT data publicly available at the website http://www.RBSP-ect.lanl.gov/. We also acknowledge the ACE SWEPAM and MAG teams for making the solar wind data available through the Goddard Space Flight Center Space Physics Data Facility (https://spdf.gsfc.nasa.gov/). We would also like to acknowledge the SpacePy project, which was used in the production of some of the figures. The authors would also like to thank S. Solomon for making the GLOW model available.

Acknowledgments
A. Glocer and M.-C. Fok acknowledge support from NASA Heliophysics Internal Scientist Funding Model (HISFM18-0006) and the Heliophysics Grand Challenge Research program (16-HGCR16_2-0008). We acknowledge valuable support from and discussion with The Center for the Unified Study of Interhemispheric Asymmetries (CUSIA). We further acknowledge valuable discussion organized by the International Space Science Institute (ISSI), particularly with the team studying cold plasma of ionospheric origin.

References

Andre, M., & Cully, C. M. (2012). Low-energy ions: A previously hidden solar system particle population. *Geophysical Research Letters*, *39*, L03101. https://doi.org/10.1029/2011GL050242

Axford, W. I. (1968). The polar wind and the terrestrial helium budget. *Journal of Geophysical Research*, *73*, 6855.

Barakat, A. R., Eccles, J. V., & Schunk, R. W. (2015). Effects of geographic-geomagnetic pole offset on ionospheric outflow: Can the ionosphere wag the magnetospheric tail? *Geophysical Research Letters*, *42*, 8288–8293. https://doi.org/10.1002/2015GL065736

Barakat, A. R., & Schunk, R. W. (2001). Effects of wave-particle interactions on the dynamic behavior of the generalized polar wind. *Journal of Atmospheric and Solar-Terrestrial Physics*, *63*, 75–83. https://doi.org/10.1016/S1364-6826(00)00106-1

Borovsky, J. E., & Steinberg, J. T. (2006). The "calm before the storm" in CIR/magnetosphere interactions: Occurrence statistics, solar wind statistics, and magnetospheric preconditioning. *Journal of Geophysical Research*, *111*, A07S10. https://doi.org/10.1029/2005JA011397

Brinton, H. C., Grebowsky, J. M., & Mayr, H. G. (1971). Altitude variation of ion composition in the midlatitude trough region: Evidence for upward plasma flow. *Journal of Geophysical Research*, *76*, 3738–3745. https://doi.org/10.1029/JA076i016p03738

Chappell, C. R., Huddleston, M. M., Moore, T. E., Giles, B. L., & Delcourt, D. C. (2008). Observations of the warm plasma cloak and an explanation of its formation in the magnetosphere. *Journal of Geophysical Research*, *113*, A09206. https://doi.org/10.1029/2007JA012945

Chappell, C. R., Moore, T. E., & Waite, J. H. (1987). The ionosphere as a fully adequate source of plasma for the Earth's magnetosphere. *Journal of Geophysical Research*, *92*, 5896–5910.

De Zeeuw, D., Sazykin, S., Wolf, R., Gombosi, T., Ridley, A., & Tóth, G. (2004). Coupling of a global MHD code and an inner magnetosphere model: Initial results. *Journal of Geophysical Research*, *109*, A12219. https://doi.org/10.1029/2003JA010366

Engwall, E., Eriksson, A. I., Cully, C. M., André, M., Torbert, R., & Vaith, H. (2009). Earth's ionospheric outflow dominated by hidden cold plasma. *Nature Geoscience*, *2*(1), 24–27.

Fok, M.-C., Buzulukova, N. Y., Chen, S.-H., Glocer, A., Nagai, T., Valek, P., & Perez, J. D. (2014). The comprehensive inner magnetosphere-ionosphere model. *Journal of Geophysical Research: Space Physics*, *119*, 7522–7540. https://doi.org/10.1002/2014JA020239

Fok, M.-C., Ebihara, Y., Moore, T. E., Ober, D. M., & Keller, K. A. (2005). *Geospace storm processes coupling the ring current, radiation belt and plasmasphere* (pp. 207–220). American Geophysical Union (AGU). https://doi.org/10.1029/159GM16

Fok, M.-C., Glocer, A., Zheng, Q., Horne, R. B., Meredith, N. P., Albert, J. M., & Nagai, T. (2011). Recent developments in the radiation belt environment model. *Journal of Atmospheric and Solar-Terrestrial Physics*, *73*, 1435–1443. https://doi.org/10.1016/j.jastp.2010.09.033

Fok, M., Wolf, R. A., Spiro, R. W., & Moore, T. E. (2001). Comprehensive computational model of Earth's ring current. *Journal of Geophysical Research*, *106*, 8417–8424. https://doi.org/10.1029/2000JA000235

Glocer, A., Dorelli, J., Toth, G., Komar, C. M., & Cassak, P. A. (2016). Separator reconnection at the magnetopause for predominantly northward and southward IMF: Techniques and results. *Journal of Geophysical Research: Space Physics*, *121*, 140–156. https://doi.org/10.1002/2015JA021417

Glocer, A., Fok, M., Meng, X., Toth, G., Buzulukova, N., Chen, S., & Lin, K. (2013). CRCM + BATS-R-US two-way coupling. *Journal of Geophysical Research: Space Physics*, *118*, 1635–1650. https://doi.org/10.1002/jgra.50221

Glocer, A., Gombosi, T. I., Toth, G., Hansen, K. C., Ridley, A. J., & Nagy, A. (2007). Polar wind outflow model: Saturn results. *Journal of Geophysical Research*, *112*, A01304. https://doi.org/10.1029/2006JA011755

Glocer, A., Khazanov, G., & Liemohn, M. (2017). Photoelectrons in the quiet polar wind. *Journal of Geophysical Research: Space Physics*, *122*, 6708–6726. https://doi.org/10.1002/2017JA024177

Glocer, A., Kitamura, N., Toth, G., & Gombosi, T. (2012). Modeling solar zenith angle effects on the polar wind. *Journal of Geophysical Research*, *117*, A04318. https://doi.org/10.1029/2011JA017136

Glocer, A., Toth, G., & Fok, M.-C. (2018). Including kinetic ion effects in the coupled global ionospheric outflow solution. *Journal of Geophysical Research: Space Physics*, *123*, 2851–2871. https://doi.org/10.1002/2018JA025241

Glocer, A., Toth, G., Gombosi, T., & Welling, D. (2009). Modeling ionospheric outflows and their impact on the magnetosphere, initial results. *Journal of Geophysical Research*, *114*, A05216. https://doi.org/10.1029/2009JA014053

Glocer, A., Tóth, G., Ma, Y., Gombosi, T., Zhang, J.-C., & Kistler, L. M. (2009). Multifluid block-adaptive-tree solar wind Roe-type upwind scheme: Magnetospheric composition and dynamics during geomagnetic storms—Initial results. *Journal of Geophysical Research*, *114*, A12203. https://doi.org/10.1029/2009JA014418

Gloeckler, G., & Hamilton, D. C. (1987). AMPTE ion composition results. *Physica Scripta*, *T18*, 73–84. https://doi.org/10.1088/0031-8949/1987/t18/009

Gombosi, T. I., & Nagy, A. F. (1989). Time-dependent modeling of field-aligned current-generated ion transients in the polar wind. *Journal of Geophysical Research*, *94*(A1), 359. https://doi.org/10.1029/JA094ia01p00359

Hoffman, J. H. (1970). Studies of the composition of the ionosphere with a magnetic deflection mass spectrometer. *International Journal of Mass Spectrometry and Ion Physics*, *4*, 315–322.

Hoffman, J. H., & Dodson, W. H. (1980). Light ion concentrations and fluxes in the polar regions during magnetically quiet times. *Journal of Geophysical Research*, *85*, 626–632. https://doi.org/10.1029/JA085iA02p00626

Hoffman, J. H., Dodson, W. H., Lippincott, C. R., & Hammack, H. D. (1974). Initial ion composition results from the Isis 2 satellite. *Journal of Geophysical Research*, *79*, 4246–4251. https://doi.org/10.1029/JA079i028p04246

Huddleston, M. M., Chappell, C. R., Delcourt, D. C., Moore, T. E., Giles, B. L., & Chandler, M. O. (2005). An examination of the process and magnitude of ionospheric plasma supply to the magnetosphere. *Journal of Geophysical Research*, *110*, A12202. https://doi.org/10.1029/2004JA010401

Keller, K. A., Fok, M., Narock, A., Hesse, M., Rastaetter, L., Kuznetsova, M. M., et al. (2005). Effect of multiple substorms on the buildup of the ring current. *Journal of Geophysical Research*, *110*, A08202. https://doi.org/10.1029/2004JA010747

Kolstø, H. M., Hesse, M., Norgren, C., Tenfjord, P., Spinnangr, S. F., & Kwagala, N. (2020). Collisionless magnetic reconnection in an asymmetric oxygen density configuration. *Geophysical Research Letters*, *47*, e2019GL085359. https://doi.org/10.1029/2019GL085359

Lee, J. H., & Angelopoulos, V. (2014). On the presence and properties of cold ions near Earth's equatorial magnetosphere. *Journal of Geophysical Research: Space Physics*, *119*, 1749–1770. https://doi.org/10.1002/2013JA019305

Lee, S. H., Zhang, H., Zong, Q.-G., Otto, A., Réme, H., & Liebert, E. (2016). A statistical study of plasmaspheric plumes and ionospheric outflows observed at the dayside magnetopause. *Journal of Geophysical Research: Space Physics*, *121*, 492–506. https://doi.org/10.1002/2015JA021540

Lemaire, J., & Scherer, M. (1970). Model of the polar ion-exosphere. *Planetary and Space Science*, *18*(1), 103–120. https://doi.org/10.1016/0032-0633(70)90070-X

Lennartsson, O. W., Collin, H. L., & Peterson, W. K. (2004). Solar wind control of Earth's H^+ and O^+ outflow rates in the 15-eV to 33-keV energy range. *Journal of Geophysical Research*, *109*, A12212. https://doi.org/10.1029/2004JA010690

Lennartsson, W., Sharp, R. D., Shelley, E. G., Johnson, R. G., & Balsiger, H. (1981). Ion composition and energy distribution during 10 magnetic storms. *Journal of Geophysical Research*, *86*, 4628–4638. https://doi.org/10.1029/JA086iA06p04628

Meng, X., Tóth, G., Glocer, A., Fok, M.-C., & Gombosi, T. I. (2013). Pressure anisotropy in global magnetospheric simulations: Coupling with ring current models. *Journal of Geophysical Research: Space Physics*, *118*, 5639–5658. https://doi.org/10.1002/jgra.50539

Meng, X., Tóth, G., Liemohn, M. W., Gombosi, T. I., & Runov, A. (2012). Pressure anisotropy in global magnetospheric simulations: A magnetohydrodynamics model. *Journal of Geophysical Research*, *117*, A08216. https://doi.org/10.1029/2012JA017791

Moore, T. E., Fok, M.-C., Chandler, M. O., Chappell, C. R., Christon, S. P., Delcourt, D. C., et al. (2005). Plasma sheet and (nonstorm) ring current formation from solar and polar wind sources. *Journal of Geophysical Research*, *110*, A02210. https://doi.org/10.1029/2004JA010563

Opher, M., Loeb, A., Drake, J., & Toth, G. (2020). A small and round heliosphere suggested by magnetohydrodynamic modelling of pick-up ions. *Nature Astronomy*, *4*, 675–683. https://doi.org/10.1038/s41550-020-1036-0

Ouellette, J. E., Lyon, J. G., Brambles, O. J., Zhang, B., & Lotko, W. (2016). The effects of plasmaspheric plumes on dayside reconnection. *Journal of Geophysical Research: Space Physics*, *121*, 4111–4118. https://doi.org/10.1002/2016JA022597

Peroomian, V., El-Alaoui, M., Abdalla, M. A., & Zelenyi, L. M. (2007). A comparison of solar wind and ionospheric plasma contributions to the september 24-25, 1998 magnetic storm. *Journal of Atmospheric and Solar-Terrestrial Physics*, *69*(3), 212–222. https://doi.org/10.1016/j.jastp.2006.07.025

Peterson, W. (2002). Ionospheric influence on substorm development. In *Proceedings of the Sixth International Conference on Substorms*, University of Washington (pp. 143).

Redmon, R. J., Peterson, W. K., Andersson, L., & Richards, P. G. (2012). Dawnward shift of the dayside O^+ outflow distribution: The importance of field line history in O^+ escape from the ionosphere. *Journal of Geophysical Research*, *117*, A12222. https://doi.org/10.1029/2012JA018145

Ridley, A., Gombosi, T., & Dezeeuw, D. (2004). Ionospheric control of the magnetosphere: Conductance. *Annales Geophysicae*, *22*, 567–584.

Schunk, R. W., & Sojka, J. J. (1997). Global ionosphere-polar wind system during changing magnetic activity. *Journal of Geophysical Research*, *102*(11), 625. https://doi.org/10.1029/97JA00292

Seki, K., Hirahara, M., Hoshino, M., Terasawa, T., Elphic, R. C., Saito, Y., et al. (2003). Cold ions in the hot plasma sheet of Earth's magnetotail. *Nature*, *422*(6932), 589–592. https://doi.org/10.1038/nature01502

Shelley, E. (1986). Magnetospheric energetic ions from the Earth's ionosphere. *Advances in Space Research*, *6*(3), 121–132. https://doi.org/10.1016/0273-1177(86)90325-X

Shelley, E., Collin, H. I., Drake, J. K., Lennartsson, W., & Yau, A. (1986). Origin of plasma sheet ions: Substorm and solar cycle dependence. *Transactions American Geophysical Union*, *67*(44), 1133. https://doi.org/10.1029/EO067i044p00867

Shelley, E. G., Johnson, R. G., & Sharp, R. D. (1972). Satellite observations of energetic heavy ions during a geomagnetic storm. *Journal of Geophysical Research*, *77*, 6104–6110. https://doi.org/10.1029/JA077i031p06104

Solomon, S. C. (2017). Global modeling of thermospheric airglow in the far ultraviolet. *Journal of Geophysical Research: Space Physics*, *122*, 7834–7848. https://doi.org/10.1002/2017JA024314

Solomon, S. C., Hays, P. B., & Abreu, V. J. (1988). The auroral 6300 emission: Observations and modeling. *Journal of Geophysical Research*, *93*(A9), 9867–9882. https://doi.org/10.1029/JA093iA09p09867

Strangeway, R. J., Ergun, R. E., Su, Y.-J., Carlson, C. W., & Elphic, R. C. (2005). Factors controlling ionospheric outflows as observed at intermediate altitudes. *Journal of Geophysical Research*, *110*, A03221. https://doi.org/10.1029/2004JA010829

Tóth, G., Ma, Y. J., & Gombosi, T. I. (2008). Hall magnetohydrodynamics on block adaptive grids. *Journal of Computational Physics*, *227*, 6967–6984. https://doi.org/10.1016/j.jcp.2008.04.010

Tóth, G., van der Holst, B., Sokolov, I. V., de Zeeuw, D. L., Gombosi, T. I., Fang, F., et al. (2012). Adaptive numerical algorithms in space weather modeling. *Journal of Computational Physics*, *231*, 870–903. https://doi.org/10.1016/j.jcp.2011.02.006

Varney, R. H., Wiltberger, M., Zhang, B., Lotko, W., & Lyon, J. (2016). Influence of ion outflow in coupled geospace simulations: 2. Sawtooth oscillations driven by physics-based ion outflow. *Journal of Geophysical Research: Space Physics*, *121*, 9688–9700. https://doi.org/10.1002/2016JA022778

Walsh, B. M., Phan, T. D., Sibeck, D. G., & Souza, V. M. (2014). The plasmaspheric plume and magnetopause reconnection. *Geophysical Research Letters*, *41*, 223–228. https://doi.org/10.1002/2013GL058802

Walsh, B. M., Sibeck, D. G., Nishimura, Y., & Angelopoulos, V. (2013). Statistical analysis of the plasmaspheric plume at the magnetopause. *Journal of Geophysical Research: Space Physics*, *118*, 4844–4851. https://doi.org/10.1002/jgra.50458

Welling, D. T., Jordanova, V. K., Zaharia, S. G., Glocer, A., & Toth, G. (2011). The effects of dynamic ionospheric outflow on the ring current. *Journal of Geophysical Research*, *116*, A00J19. https://doi.org/10.1029/2010JA015642

Wiltberger, M., Lotko, W., Lyon, J. G., Damiano, P., & Merkin, V. (2010). Influence of cusp O^+ outflow on magnetotail dynamics in a multifluid MHD model of the magnetosphere. *Journal of Geophysical Research*, *115*, A00J05. https://doi.org/10.1029/2010JA015579

Winglee, R. M., Chua, D., Brittnacher, M., Parks, G. K., & Lu, G. (2002). Global impact of ionospheric outflows on the dynamics of the magnetosphere and cross-polar cap potential. *Journal of Geophysical Research*, *107*(A9), 1237. https://doi.org/10.1029/2001JA000214

Zhang, B., Brambles, O. J., Wiltberger, M., Lotko, W., Ouellette, J. E., & Lyon, J. G. (2016). How does mass loading impact local versus global control on dayside reconnection? *Geophysical Research Letters*, *43*, 1837–1844. https://doi.org/10.1002/2016GL068005

Zhao, K., Kistler, L. M., Lund, E. J., Nowrouzi, N., Kitamura, N., & Strangeway, R. J. (2020). Factors controlling O^+ and H^+ outflow in the cusp during a geomagnetic storm: Fast/teams observations. *Geophysical Research Letters*, *47*, e2020GL086975. https://doi.org/10.1029/2020GL086975